Spin-orbit-torque-enabled three-dimensional magnetic field sensor with low offset and high sensitivity

Sebastian Zeilinger*
Physics of Functional Materials, Faculty of Physics, University of Vienna, Vienna, Austria
Research Platform MMM Mathematics-Magnetism-Materials, University of Vienna, Vienna, Austria and
Vienna Doctoral School in Physics, University of Vienna, Vienna, Austria

Johannes Güttinger and Armin Satz
Infineon Technologies AG, Villach, Austria

Klemens Prügl and Michael Kirsch
Infineon Technologies AG, Regensburg, Germany

Joshua M. Salazar-Mejía
Vienna Doctoral School in Physics, University of Vienna, Vienna, Austria

Sabri Koraltan
Institute of Applied Physics, Technische Universität Wien, A-1040 Vienna, Austria

Philip Heinrich, Bernd Aichner, and Florian Bruckner
Physics of Functional Materials, Faculty of Physics, University of Vienna, Vienna, Austria

Sophie Zeilinger
Faculty Center for Nano Structure Research, Faculty of Physics, University of Vienna, Vienna, Austria

Hubert Brückl
Department for Integrated Sensor Systems, University for Continuing Education Krems, 2700 Wiener Neustadt, Austria

Dieter Suess
Physics of Functional Materials, Faculty of Physics, University of Vienna, Vienna, Austria and
Research Platform MMM Mathematics-Magnetism-Materials, University of Vienna, Vienna, Austria

(Received 31 July 2025; revised 16 October 2025; accepted 21 November 2025; published 11 December 2025)

In this work we demonstrate a spin-orbit-torque (SOT) magnetic field sensor, designed as a Ta/CoFeB/MgO structure, with high sensitivity and capable of active offset compensation in all three spatial directions. This is described and verified in experiment and simulation. The measurements of magnetic fields showed an offset of 35, 42, and 3 μT for x-, y-, and z-fields respectively. Furthermore, the sensitivities of these measurements had values of 590, 580, and 490 $\mathrm{V\,A^{-1}\,T^{-1}}$ in the x-, y-, and z-direction, respectively. In addition, the robustness to bias fields is demonstrated via experiments and single-spin simulations by applying bias fields in the y-direction. Cross sensitivities were further analyzed via single-spin simulations, performing a parameter sweep of different bias fields in the y- and z-direction up to ±1 mT. The extraction of the SOT parameters η_{DL} and η_{FL} is shown via an optimization of a single-spin curve to the experimental measurements.

DOI: 10.1103/997y-hk7m

*Contact author: sebastian.zeilinger@univie.ac.at

I. INTRODUCTION

Magnetic field sensors are a fundamental part of our modern-day society. They are used in various systems, including but not limited to automobiles , cell phones, and robotics. In multiple applications such as electric current sensors via magnetic fields, it is required to measure the absolute value of the magnetic field with the highest accuracy. Here, the zero-field offset is the main limiting factor in state-of-the-art sensors.

On the one hand, a big part of today's magnetic field sensors are Hall-based devices that use the spinning-current technique to achieve active offset compensation in the microtesla range [1,2]. On the other hand, magnetoresistive devices, such as tunneling magnetoresistance sensors, offer very high signal-to-noise ratios but typically lack offset compensation [3–6].

In this work we utilize a modulation principle of the magnetization to reduce the offset. This is realized by spin orbit torque (SOT) that is highly energy efficient and allows for integration into standard CMOS techniques. The SOT effect is under intense focus due to the potential applications in memory and sensor applications [7–9]. Efforts have recently been made to utilize the current-induced SOT effect for magnetic field sensing devices [10–12]. We present a sensor based on this effect, designed with active offset compensation. In contrast to Refs. [12] and [13], our sensor is also able to measure z-fields offset-free, which enables a true three-dimensional (3D) sensor using only one sensitive element. Offset compensation in the z-direction is achieved through the spinning-current technique, commonly used in conventional Hall devices [14,15].

II. THEORY

The geometry of the device studied is conceived as a crosslike structure with an overall length of 10 µm and a width of the individual arms of 2 µm [see Fig. 1(a)]. The sensor is composed of a ferromagnetic (FM) layer of $Co_{60}Fe_{20}B_{20}$ (1 nm) deposited on a heavy metal (HM) layer of Ta (6 nm), which is in the β-phase. A MgO (1.5 nm)/Ta (5 nm) heterostructure is subsequently deposited over the active layers, although this is not depicted in Fig. 1(a). The whole stack is Ta (6 nm)/$Co_{60}Fe_{20}B_{20}$ (1 nm)/MgO (1.5 nm)/Ta (5 nm), with the applied current flowing in the Ta (6 nm)/$Co_{60}Fe_{20}B_{20}$ (1 nm) bilayer. This design enables the measurement of the perpendicular voltage (V_{xy}) in response to an electrical current (I_{xx}) [see Fig. 1(a)].

In order to describe the sensor principle we use the Landau-Lifshitz-Gilbert equation augmented with the SOT torque:

$$\partial_t \mathbf{m} = -\gamma \mathbf{m} \times \mathbf{H}^{\text{eff}} + \alpha \mathbf{m} \times \partial_t \mathbf{m} + \mathbf{T}. \tag{1}$$

Here γ is the gyromagnetic ratio, α the Gilbert damping factor, and $\mathbf{H}^{\text{eff}}$ the effective magnetic field. The torque term $\mathbf{T}$ [16], given by

$$\mathbf{T} = \gamma H_{\text{FL}} \mathbf{m} \times \mathbf{p} + \gamma H_{\text{DL}} \mathbf{m} \times (\mathbf{m} \times \mathbf{p}), \tag{2}$$

is orthogonal to the magnetization and can be expressed as a fieldlike (FL) part (first term) and a dampinglike (DL) part (second term). The spin polarization is expressed with $\mathbf{p}$, which points in the positive y-direction ($\mathbf{p} = (0, 1, 0)^{\text{T}}$) [see Fig. 1(b)]. H_{DL} and H_{FL} represent the amplitudes of the field components corresponding to the two distinct parts, which can be expressed over the SOT coefficients η_{FL} and η_{DL} as [10]

$$H_{\text{DL/FL}} = p_f \cdot \eta_{\text{DL/FL}}, \tag{3}$$

with

$$p_f = \frac{j_e \hbar}{2e\mu_0 t M_s}. \tag{4}$$

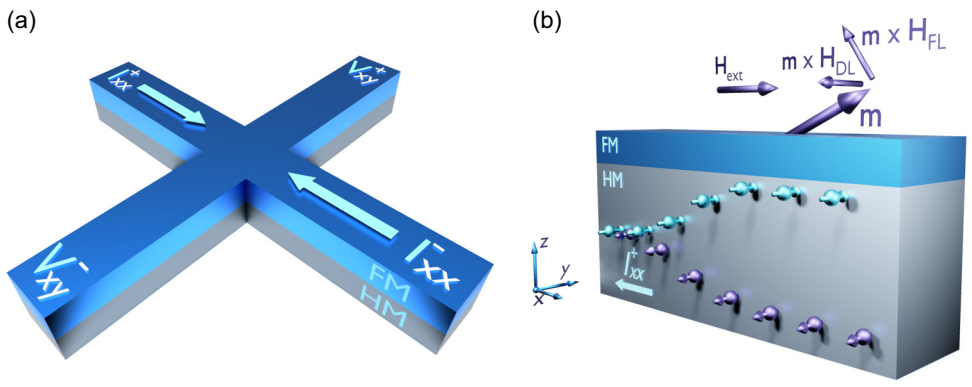

FIG. 1. (a) The device analyzed is designed as a crosslike structure, with a ferromagnetic layer on top of a heavy metal layer. (b) Spin separation via the spin Hall effect . Spin polarized current acts like a torque, through the components $\mathbf{m} \times \mathbf{H}_{\text{DL}}$ and $\mathbf{m} \times \mathbf{H}_{\text{FL}}$, on the magnetization of the ferromagnetic (FM) layer under the influence of an external magnetic field ($\mathbf{H}_{\text{ext}}$).

Here j_e is the electrical current density flowing through the HM layer, t the thickness of the FM layer, and M_s the saturation magnetization of the FM layer.

The torque term $\mathbf{T}$ in Eq. (2) can be inserted into Eq. (1) as field contributions [$\mathbf{H}_{\mathrm{FL}} = H_{\mathrm{FL}}\mathbf{p}$ and $\mathbf{H}_{\mathrm{DL}} = H_{\mathrm{DL}}\mathbf{m} \times \mathbf{p}$, with $\mathbf{m} \times \mathbf{H}_{\mathrm{DL/HL}}$ visible in Fig. 1(b)] which act on the magnetization of the FM layer [17]:

$$\partial_t \mathbf{m} = -\gamma \mathbf{m} \times \left(\mathbf{H}^{\mathrm{eff}} - H_{\mathrm{FL}}\mathbf{p} - H_{\mathrm{DL}}\mathbf{m} \times \mathbf{p}\right) + \alpha \mathbf{m} \times \partial_t \mathbf{m}. \tag{5}$$

With the magnetization initially aligned along x by the external magnetic field, the dampinglike torque acts as an effective field along z, resulting in an out-of-plane (OOP) magnetization. Simultaneously, the fieldlike torque relaxes the magnetization toward $\pm y$, depending on the SOT current direction. If the current direction is flipped in the other direction, H_{DL} and H_{FL} change signs, leading to opposite OOP magnetization. This can be described by analytically solving Eq. (5) in the linear regime, assuming small fields in the x- and/or z-directions (H_x, H_z), and a vanishing field in the y-direction ($H_y = 0$). The detailed calculation can be seen in Appendix A, which leads to

$$m_{z,I\pm} = \frac{\mp H_x \left|p_f\right| \eta_{\mathrm{DL}} + H_z(\left|p_f\right| \eta_{\mathrm{FL}})}{\left(\left|p_f\right| \eta_{\mathrm{DL}}\right)^2 + (\left|p_f\right| \eta_{\mathrm{FL}})(\left|p_f\right| \eta_{\mathrm{FL}} - H_k)}. \tag{6}$$

Here H_k is the amplitude of the anisotropy field pointing in the z-direction. It can be seen that if the z-magnetization ($m_{z,I-}$) with negative current is subtracted from the z-magnetization with positive current ($m_{z,I+}$) the response is only sensitive to H_x-fields to first order, canceling any cross sensitivities. The signal corresponding to external x-fields (S_x) therefore takes the form

$$\begin{aligned} S_x(H_x) &= \frac{R_s}{2} \cdot \left(m_{z,I+} - m_{z,I-}\right) \\ &= -R_s \frac{\eta_{\mathrm{DL}} H_x}{-\eta_{\mathrm{FL}} H_k + (\eta_{\mathrm{DL}}^2 + \eta_{\mathrm{FL}}^2)\left|p_f\right|}. \end{aligned} \tag{7}$$

Here R_s is the anomalous Hall coefficient, used to convert the equation into units of ohms (see Sec. VIII B). This factor was introduced to compare simulation data with measured data. Alternatively, if the magnetizations from the two cases are added, the H_x component is canceled, leaving the system sensitive primarily to external H_z-fields of first order. This yields the signal for z-fields (S_z), which allows the measurement of external fields without sensitivities in other directions:

$$\begin{aligned} S_z(H_z) &= \frac{R_s}{2} \cdot \left(m_{z,I+} + m_{z,I-}\right) \\ &= R_s \frac{\eta_{\mathrm{FL}} H_z}{-\eta_{\mathrm{FL}} H_k + (\eta_{\mathrm{DL}}^2 + \eta_{\mathrm{FL}}^2)\left|p_f\right|}. \end{aligned} \tag{8}$$

III. MEASUREMENT OF THREE-DIMENSIONAL MAGNETIC FIELDS

To measure an external magnetic field using the SOT effect, the anomalous Hall resistance $R_{xy} = V_{xy}/I_{xx}$ was determined from the anomalous Hall voltage (V_{xy}), which was measured perpendicular to the current flow (I_{xx}^{+}) [see Fig. 1(a)] [18]. Since this method is sensitive to OOP magnetization, the anomalous Hall resistance is proportional to m_z. As mentioned earlier, to eliminate cross sensitivities, the SOT current direction is reversed, and the subtraction of both resistance values yields the final signal. This approach also has the advantage that any electrical offset present in the measurement is canceled out, resulting in an offset-compensated signal. This occurs because the offset remains constant for both current directions, leading to a cancelation when subtracting the two cases, which can be seen in Figs. 2(a) and 2(b). An external H_x-field can therefore be determined using Eq. (7), represented by the blue data in Fig. 2(d). By substituting Eq. (19) into Eq. (7), the expression can be rewritten in terms of R_{xy}, which is directly measurable:

$$S_x = \frac{1}{2} \cdot \left(R_{xy}\left(I_{xx}^{+}\right) - R_{xy}\left(I_{xx}^{-}\right)\right). \tag{9}$$

Here $R_{xy}\left(I_{xx}^{\pm}\right)$ is the anomalous Hall resistance for the positive/negative SOT current direction. Due to symmetry, it is possible to obtain the signal for external H_y-fields in the same way, illustrated as the blue curve with squares in Fig. 2(e):

$$S_y = \frac{1}{2} \cdot \left(R_{yx}\left(I_{yy}^{+}\right) - R_{yx}\left(I_{yy}^{-}\right)\right). \tag{10}$$

In this case the SOT current is applied in the y-direction, denoted by I_{yy}, and the anomalous Hall voltage measured in the x-direction (V_{yx}). In the analytical expression (7), this case can be evaluated simply by exchanging x and y.

For measuring external z-fields, Eq. (8) can be used, where any cross sensitivities are canceled out due to the summation of $m_{z,I+}$ and $m_{z,I-}$. However, this does not result in offset compensation, which is more challenging, as the signal does not reverse when the direction of the SOT current is changed [see Eq. (8) and Fig. 2(c)]. In other literature such as Ref. [12], the H_z-field was obtained by adding up the anomalous Hall effect (AHE) resistances for $\pm I_{xx}$ or $\pm I_{yy}$ as in Eq. (8), which does not lead to an offset compensation for the measurement of H_z-fields. Additionally, in Ref. [13], the measurement of external z-fields lacks offset compensation, and it was noted that the remaining offset was subtracted from the data manually. In contrast, we employ a compensation method similar to the spinning-current principle used in commercial Hall

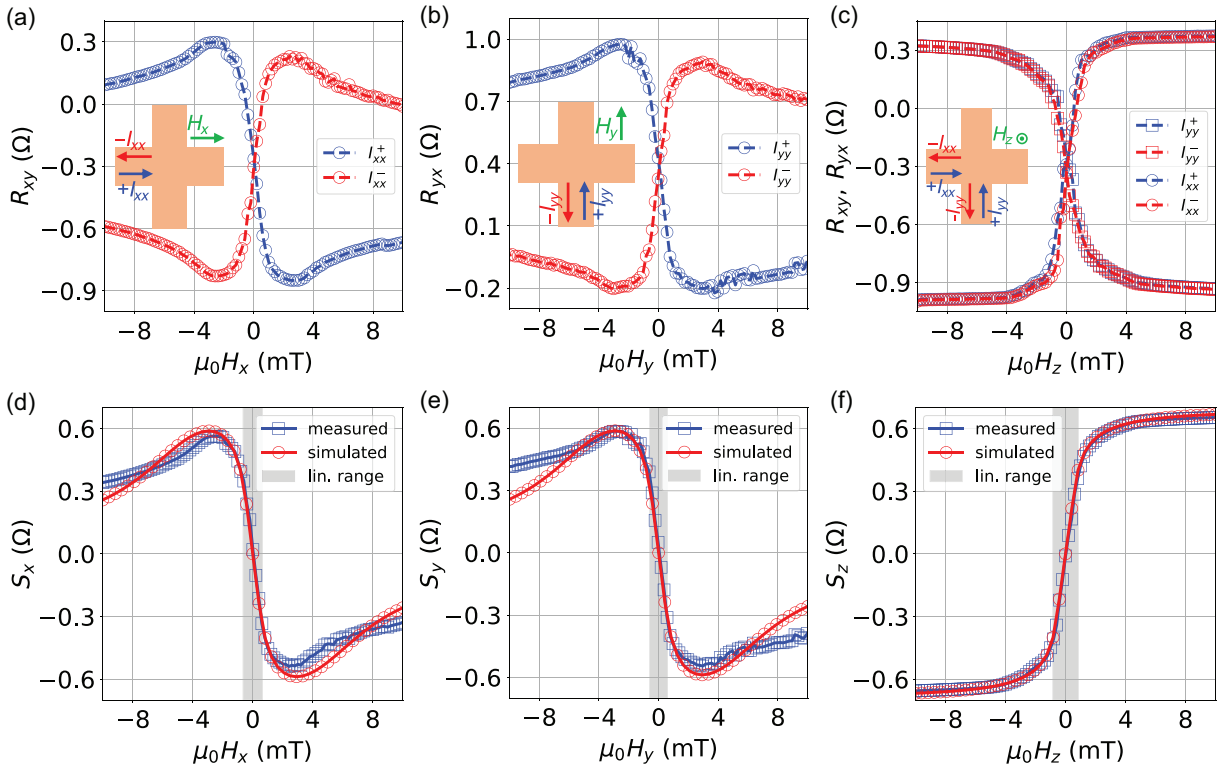

FIG. 2. (a) Measured R_{xy} for 2.7 mA current strength under external H_x-fields for I_{xx}^{+} (blue dashed curve with circles) and I_{xx}^{-} (red dashed curve with circles). (b) Measured R_{yx} for 2.7 mA current strength under external H_y-fields. (c) Measured R_{xy} and R_{yx} for 2.7 mA current strength under external H_z-fields for $I_{xx}^{\pm}$ (dashed curves with circles) and $I_{yy}^{\pm}$ (dashed curves with rectangles). (d) The sensor response (blue curve with squares) for 2.7 mA current strength and single-spin simulation results (red curve with circles) under external H_x-fields. The linear range is shown as the grey shaded area. (e) The same plot but for an external H_y-field sweep. (f) The response under external H_z-fields.

sensors [14,15]:

$$S_z = \frac{1}{2} \cdot \left(\left(\frac{R_{xy}\left(I_{xx}^{+}\right) + R_{xy}\left(I_{xx}^{-}\right)}{2} \right) - \left(\frac{R_{yx}\left(I_{yy}^{+}\right) + R_{yx}\left(I_{yy}^{-}\right)}{2} \right) \right). \tag{11}$$

Summing the anomalous Hall resistances of I_{xx}^{+} and I_{xx}^{-} as well as I_{yy}^{+} and I_{yy}^{-}, rather than subtracting them, eliminates the SOT contributions from the signal. Subsequently, a standard spinning-current technique can be applied, by subtracting the two remaining terms. This allows an offset compensated measurement of external magnetic fields in all three directions, which is visible in Figs. 2(d)–2(f). The experimental data were acquired using a current density of $j_e = 1.71 \cdot 10^{11}\,\mathrm{A\,m^{-2}}$ ($I_{xx} = 2.7\,\mathrm{mA}$), under an external magnetic field ranging from $\mu_0 H_{\mathrm{ext}} = -10\,\mathrm{mT}$ to 10 mT. The reported current density j_e refers specifically to the value within the HM layer, while the value in parentheses indicates the total current applied across the Ta/CoFeB bilayer. Details regarding the calculation of the current density are provided in Sec. VIII D. The recording time was $t_r = 0.5\,\mathrm{s}$ for each measurement.

The sensitivity or slope (κ_i can be extracted within the linear range, utilizing the equation

$$\kappa_i = \frac{1}{R_s} \frac{dS_i}{dH_i}\,[\mathrm{mA^{-1}}]. \tag{12}$$

Here, R_s represents the anomalous Hall coefficient, which, in our case, is $R_s = 0.687\,\Omega$ [19] (see Sec. VIII B). Since the sensitivities were measured in units of $\mathrm{V\,A^{-1}\,T^{-1}}$, we define $\xi_i = (R_s/\mu_0)\kappa_i$ to match the commonly used units and simplify notation, accepting that both κ_i and ξ_i represent sensitivity in different unit systems.

To extract the values from the experimental data an iterative symmetric-fitting algorithm was used. Starting with symmetric data points around zero magnetic field, a linear regression was performed and compared to the next outer data pair. If the relative deviation δ_r, defined as

$$\delta_r = \frac{|V_{\mathrm{meas}} - V_{\mathrm{fit}}|}{|V_{\mathrm{meas}}|}, \tag{13}$$

was below 10%, the fitting window was expanded and the process repeated. Here V_{meas} is the measured voltage

and V_{fit} the fitted voltage. The iteration stopped once this criterion was no longer met. The resulting slope provides the sensitivity, the intercept gives the field offset, and the largest accepted symmetric field interval ($\pm\mu_0 H_{\mathrm{max}}$) defines the linear range. For all three sensor axes, the algorithm was initialized with an initial window of $\pm 0.3\,\mathrm{mT}$. Using this approach, the linear range was found to be $\pm 0.65\,\mathrm{mT}$ in the x-direction, $\pm 0.6\,\mathrm{mT}$ in the y-direction, and $\pm 0.85\,\mathrm{mT}$ in the z-direction, which is also shown in Figs. 2(d)–2(f). The extracted sensitivity values of the sensor for the presented data are $\xi_x = -590\,\mathrm{V\,A^{-1}\,T^{-1}}$ $(-1.59\,\mathrm{V/T})$ in the x-direction, $\xi_y = -580\,\mathrm{V\,A^{-1}\,T^{-1}}$ $(-1.57\,\mathrm{V/T})$ in the y-direction, and $\xi_z = 490\,\mathrm{V\,A^{-1}\,T^{-1}}$ $(1.32\,\mathrm{V/T})$ in the z-direction. The values in the parentheses were multiplied by the current strength to show the sensitivities also in units of $\mathrm{V\,T^{-1}}$. For comparison, commercially available tunnel magnetoresistance (TMR) sensors exhibit significantly higher performance metrics. For example, an Infineon TMR sensor reports a linear range of 35 mT and a sensitivity of $9 \times 10^4\,\mathrm{V\,A^{-1}\,T^{-1}}$ [10]. The device studied here exhibits a more limited linear range and sensitivity, but in contrast enables active offset compensation in all three spatial dimensions. Additional sensitivities reported in the literature can be found in Ref. [10]. The offset (o_i) performance of the sensor for vanishing field was $o_x = 35\,\mu\mathrm{T}$ in the x-direction, $o_y = 42\,\mu\mathrm{T}$ in the y-direction, and $o_z = 3\,\mu\mathrm{T}$ in the z-direction, without shielding from the Earth's magnetic field.

To illustrate the thermal effects on the sensor behavior, measurements under external x- and z-fields up to 40 mT at different SOT current strengths are included in Appendix D, where the influence of temperature is analyzed in detail.

To validate these results, the experimental data were compared with single-spin simulations, shown as red circles in Figs. 2(d)–2(f). It can be seen that the simulation agrees well with the experiment within the linear range. For the cases with external in-plane (IP) fields the simulation deviates slightly for higher external fields.

The parameters used for the simulations were $\gamma = 2.2128 \cdot 10^5\,\mathrm{mA^{-1}\,s^{-1}}$, $\alpha = 0.01$ [20,21], $M_s = 1.2/\mu_0\,\mathrm{A\,m^{-1}}$, $j_e = 1.71 \cdot 10^{11}\,\mathrm{A\,m^{-2}}$, $H_k = 3049\,\mathrm{A\,m^{-1}}$, $t = 1\,\mathrm{nm}$, $\eta_{\mathrm{FL}} = 0.0360$, and $\eta_{\mathrm{DL}} = 0.0436$. The anisotropy field H_k and the SOT efficiency parameters η_{DL} and η_{FL} were extracted from the experimental data using the analytical approach described in the following section. With these values and Eq. (4), one obtains $p_f = 46\,898\,\mathrm{A\,m^{-1}}$. Unless stated otherwise, these parameters were used for all simulations.

IV. EXTRACTION OF SOT PARAMETERS

A key challenge that arose during this process was the lack of knowledge about the SOT efficiency parameters (η_{FL}, η_{DL}) and the anisotropy field (H_k). Equations (7) and (8), which connect these three parameters, can be utilized to determine these values. This approach assumes that the FM layer can be modeled as a single-spin system and that the magnetization turns for sufficiently high SOT current with vanishing external field into the negative y-direction (see Appendices A and B).

From these equations one can derive the following formulas for η_{FL} and η_{DL}:

$$\eta_{\mathrm{FL}} = \frac{\kappa_z + H_k \kappa_z^2}{|p_f|\left(\kappa_x^2 + \kappa_z^2\right)}, \tag{14}$$

$$\eta_{\mathrm{DL}} = \frac{-\kappa_x - H_k \kappa_x \kappa_z}{|p_f|\left(\kappa_x^2 + \kappa_z^2\right)}, \tag{15}$$

which only depend on the slopes κ_x and κ_z and the anisotropy field H_k. Since the slopes are determined from the experimental data ($\xi_i = (R_s/\mu_0)\,\kappa_i$), the only remaining unknown is H_k, which can thus be determined.

To calculate the value for the anisotropy field the following scheme was used. Single-spin simulations are carried out, with the SOT parameters defined over the analytical equations (14) and (15). The absolute difference between the measured and simulated curves within an external field range of $\pm 10\,\mathrm{mT}$ is minimized by adjusting the H_k value, which also determines the values of η_{FL} and η_{DL}. Because the slope is fixed in the analytical solution, it does not change with a change in H_k. The code optimizes the behavior beyond the linear range. This process was performed simultaneously for the data with external H_x- and H_z-fields, shown in Figs. 2(d) and 2(f). An initial interval was selected for the anisotropy field H_k. The algorithm identified the optimal value with the smallest deviation from the measured signal, by evaluating equidistant points within the initial interval, then creating a smaller interval around this value and repeating the process. This procedure was iterated five times in total. A detailed mathematical formulation of the optimization algorithm can be found in Appendix C.

Utilizing Eqs. (15) and (14), the values for η_{DL} and η_{FL} were calculated:

$$\begin{aligned} \mu_0 H_k &= 3.83\,\mathrm{mT}, \\ \eta_{\mathrm{DL}} &= 0.0436, \\ \eta_{\mathrm{FL}} &= 0.0360. \end{aligned} \tag{16}$$

The final outcome of the extraction is illustrated in the simulation results of Figs. 2(d)–2(f), which show the comparison between simulation and experiment. The strength of the perpendicular magnetic anisotropy essentially results from the balance of the perpendicular interface anisotropy and the IP shape anisotropy. The behavior of the anisotropy as a function of temperature for different SOT current strengths for a different sample is shown in

Appendix D. Additionally, the anisotropy field is extracted there for two different current amplitudes.

V. MAGNETIZATION STATE

In the analytical solution, it was assumed that the magnetization could be approximated as a single-spin system. Consequently, analyzing the magnetization state of the FM layer is crucial. In the experiment, the resistance $R_{xx} = V_{xx}/I_{xx}$ along the current flow was measured with a standard four probe configuration to minimize the influence of contact resistance. (see Fig. 3). For the measurement a current density of $j_e = 1.84 \cdot 10^{11}\,\mathrm{A\,m^{-2}}$ ($I_{xx} = 2.9\,\mathrm{mA}$) and an external field between $\pm 10\,\mathrm{mT}$ was applied in the x-direction. The current pulse time was $dt = 0.3\,\mathrm{s}$ and the recording time was $t_r = 0.25\,\mathrm{s}$. A clear effect is visible between $\pm 4\,\mathrm{mT}$ in the measurement, where the R_{xx} values go down from $1070.55\,\Omega$ to $1070.46\,\Omega$ [see Fig. 3(a)]. Reference [22] reports a change in R_{xx} due to a dependency on the magnetization direction in W/CoFeB/MgO heterostructures, which can be explained mainly by spin Hall magnetoresistance (SMR $\propto \left(1 - m_y^2\right)$). In addition, anisotropic magnetoresistance (AMR $\propto m_x^2$) arises in the system but is reported to be negligible. To examine the magnetization of the FM layer in greater detail, single-spin and micromagnetic simulations were performed [see Fig. 3(b)]. For the micromagnetic simulations, the GPU-enhanced finite-difference simulation software, MAGNUMNP, was utilized [23]. The simulation parameters for the micromagnetic simulation were $A_{\mathrm{ex}} = 1.3686 \cdot 10^{-11}\,\mathrm{J\,m^{-1}}$, $K_u = 5.7479 \cdot 10^{5}\,\mathrm{J\,m^{-3}}$, $\mathbf{k} = (0, 0, 1)^{\mathrm{T}}$, and $D = 0.06 \cdot 10^{-3}\,\mathrm{J\,m^{-2}}$, taken from Ref. [24]. Here, A_{ex} represents the exchange stiffness, K_u the uniaxial anisotropy constant, $\mathbf{k}$ the anisotropy axis, while D denotes the Dzyaloshinskii–Moriya interaction (DMI) coefficient. We computed the uniaxial anisotropy constant K_u from the extracted anisotropy field H_k. Using the saturation magnetization M_s, the uniaxial anisotropy constant can be expressed as (see Ref. [25])

$$K_u = \frac{\mu_0 H_k M_s}{2} + \frac{\mu_0 M_s^2}{2}. \tag{17}$$

The first term represents the intrinsic uniaxial anisotropy, while the second term accounts for the shape (demagnetization) contribution, which is particularly relevant for thin films. The values for the SOT parameters were taken from the extraction mentioned in Eq. (16). The remaining parameters are the same as in the single-spin simulation. The SMR effect is visualized as the blue data, with a solid line and circular markers for the single-spin simulation. The dotted lines with point markers denote the micromagnetic simulations. In the simulation, the SMR effect is limited to $\pm 4\,\mathrm{mT}$ external magnetic field with a sharp peak for the single-spin simulation. The AMR effect visualized in red has a wider range without a peak for single-spin and micromagnetic simulations. The shape and range of the experimental data agree with the simulated SMR effect and hint at a negligible AMR effect, agreeing with Ref. [22]. For the SMR the resistance scales with $1 - m_y^2$, leading to lowest resistance values for a maximum m_y^2 magnetization and therefore parallel/antiparallel alignment to the spin polarization. The micromagnetic simulation only shows a partial dip in $1 - m_y^2$, not agreeing with the assumption of the analytical solution. Since the correlation between the resistance decrease and the m_y magnetization in the sample is unknown, a definitive conclusion on the magnetization state cannot be drawn.

To better understand this, we compare the data from the micromagnetic simulation, performed under an external magnetic field sweep in the x-direction in the range $\mu_0 H_x = \pm 10\,\mathrm{mT}$, with a single-spin simulation. This comparison is illustrated in Fig. 4(a), where the single-spin

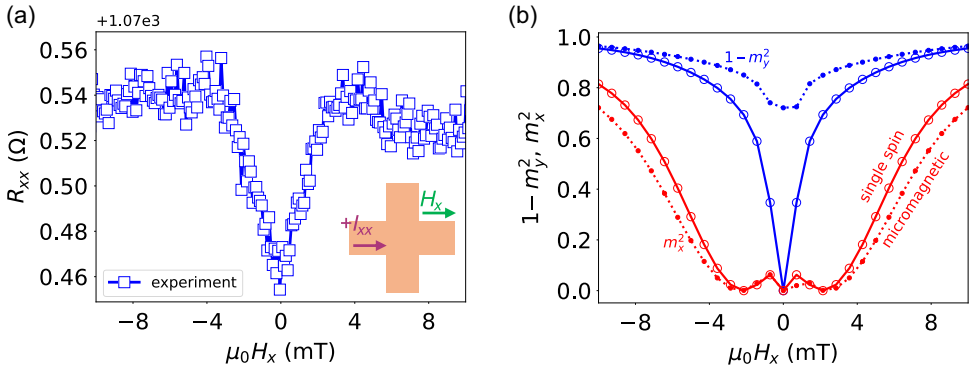

FIG. 3. (a) Measured R_{xx} data over an external H_x-field. The reduced resistance due to the combined anisotropic magnetoresistance (AMR) and spin Hall magnetoresistance (SMR) effect around weak external H_x-fields is visible. (b) The result of the single-spin simulation (solid lines with circular markers) and the micromagnetic simulation (dotted lines with point markers) of the same situation. The AMR effect ($\propto m_x^2$) is plotted as the red curve and the SMR effect ($\propto (1 - m_y^2)$) as the blue curve over the external H_x-field.

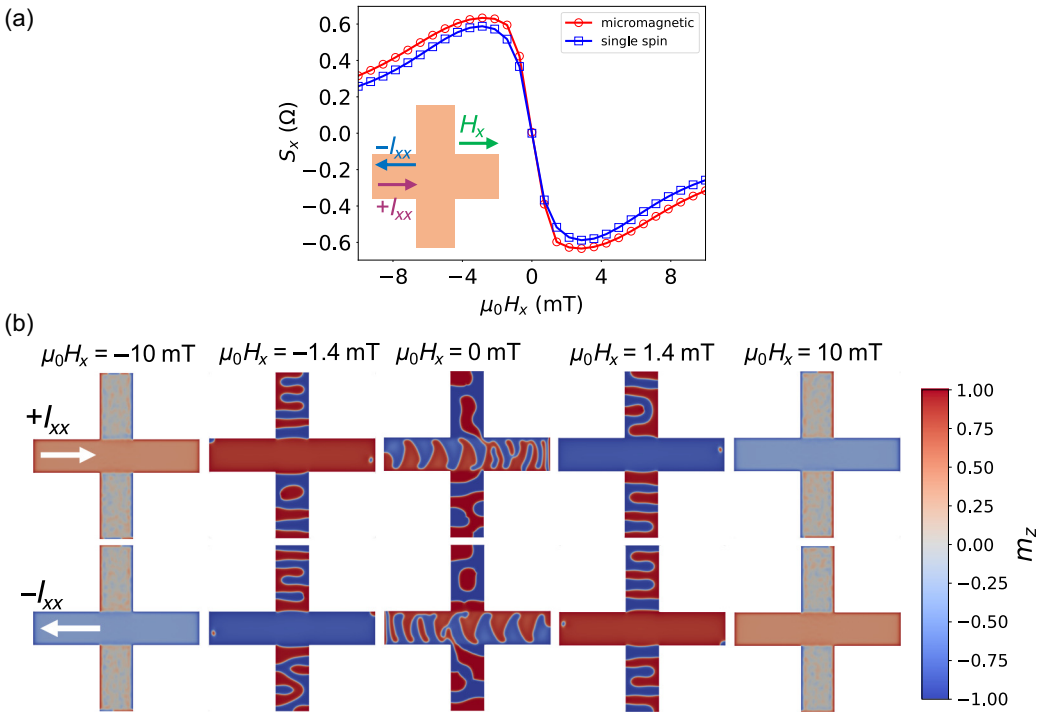

FIG. 4. (a) Comparison of S_x over an external H_x-field sweep of the single-spin simulation (blue curve) and the micromagnetic simulation (red curve) with an applied SOT current density $j_e = 1.71 \cdot 10^{11}\,\mathrm{A\,m^{-2}}$. (b) Snapshots of the micromagnetic simulation over an external H_x-field sweep for positive (top row) and negative (bottom row) SOT current. The m_z-component of the magnetization for the same H_x-field sweep is visualized. Blue areas denote negative magnetization values and red positive values, which can be seen in the colorbar on the right.

simulation (blue curve) and the micromagnetic simulation (red curve) are shown. The calculated signal is plotted as a function of the external H_x-field. The micromagnetic simulation shows good agreement with the single-spin simulation, albeit with a slightly increased amplitude. In Fig. 4(b) snapshots of the m_z magnetization for different H_x-field values and different SOT current directions can be seen. Blue areas denote negative magnetization values and red areas positive magnetization values, visualized in the colorbar on the right in Fig. 4(b). The top row shows snapshots for positive SOT currents, while the bottom row corresponds to negative SOT currents. The cross-sectional views reveal that, at low external fields ($|\mu_0 H_x| < 1.4\,\mathrm{mT}$), the magnetization adopts a multidomain OOP state with a limited IP magnetization [see also Fig. 3(b)]. This behavior deviates from the assumption of a uniform single-spin system and thus does not align with the results of single-spin simulations. The split in multiple domains explains the big difference in SMR effect between single-spin and micromagnetic simulations [see Fig. 3(b), blue lines].

Nevertheless, in the region $|\mu_0 H_x| \leq 1.4\,\mathrm{mT}$, the signals from both the single-spin and micromagnetic simulations exhibit good agreement. This correspondence arises because the combined effects of SOT and DMI induce domain wall motion that shifts the domains outwards, effectively resulting in a single-domain state [26]. In the limit of vanishing external fields, a multidomain state emerges with compensating domains, forming wavelike patterns driven by the combined SOT and DMI effects. These domains move under the SOT current, being annihilated on one side while created on the other, such that their contributions to the signal nearly cancel. Consequently, consistency is observed in this regime as well [see Fig. 4(b)].

VI. BEHAVIOR UNDER BIAS FIELDS

For a 3D magnetic field sensor, the cross sensitivities of all three field components have to be investigated. On the one hand, there is the possibility of IP bias fields while measuring OOP fields. On the other hand, there are IP and OOP bias fields when an IP component (x or y) is measured. Low cross sensitivity is a prerequisite for the simultaneous measurement of magnetic fields in any arbitrary direction. In Fig. 5(a) the case for an IP field (x-field) measurement with an IP bias field in the y-direction is shown. The measured anomalous Hall resistances $R_{xy}(I_{xx}^{+})$ and $R_{xy}(I_{xx}^{-})$ are visualized for the cases without (blue data) and with bias field ($\mu_0 H_y = 0.5\,\mathrm{mT}$, red data). A current density $j_e = \pm 1.71 \cdot 10^{11}\,\mathrm{A\,m^{-2}}$ ($I_{xx} = \pm 2.7\,\mathrm{mA}$) was applied for a pulse length $dt = 0.6\,\mathrm{s}$. The recording time

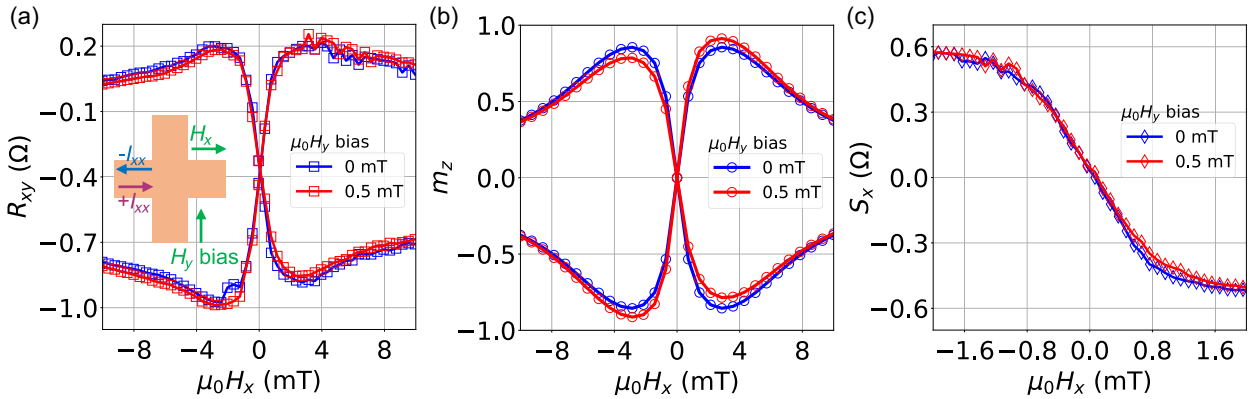

FIG. 5. (a) The measured response curve for an external H_x-field sweep, with zero bias field (blue curve with squares) and $\mu_0 H_y = 0.5\,\mathrm{mT}$ bias field (red curve with squares), for SOT current in the $\pm x$-direction. (b) The simulated data for the same two cases, utilizing a single-spin simulation. (c) The calculated sensor curve for the measured data, using Eq. (9).

was set to $t_r = 0.5\,\mathrm{s}$ and the external $\mu_0 H_x$-field was swept from $\mu_0 H_{\mathrm{ext}} = 10\,\mathrm{mT}$ to $-10\,\mathrm{mT}$.

The data measured under the influence of a transverse bias field in the y-direction reveal an increased amplitude of the AHE signal for one SOT current polarity and a decreased amplitude for the opposite polarity. This asymmetry arises from the interplay between the fieldlike torque and the transverse bias field, which together influence the equilibrium configuration of the magnetization. As visible in Eq. (A10) in Appendix A, the OOP magnetization component m_z in the presence of an x-directed external field is inversely proportional to a denominator that depends on the difference between the fieldlike torque and the applied bias field H_y. When the bias field and the fieldlike torque act in the same direction, their combined effect reduces the denominator, enhancing m_z and thereby increasing the AHE signal. Conversely, if they partially cancel, the denominator becomes larger, reducing the effective canting and leading to a weaker AHE response.

This can be seen in the red curve of Fig. 5(a). For the signal, starting at top left, the amplitude of the red curve is slightly lower compared to the blue curve. The opposite happens for the signal with opposite current direction, where the amplitude is increased. For comparison a single-spin simulation of the system was performed, which is visible in Fig. 5(b). The z-magnetization is visualized over an external H_x-field sweep for the same two cases, without bias field (blue curve with circles) and with $\mu_0 H_y = 0.5\,\mathrm{mT}$ bias field (red curve with circles). Also in the simulation, the amplitude increases for one current direction and decreases for the other direction, as in the experiment.

In Fig. 5(c), the signal (S_x) is plotted as a function of the external H_x-field. The cases with no bias field (blue curve with diamonds) and with a bias field of $\mu_0 H_y = 0.5\,\mathrm{mT}$ (red curve with diamonds) are shown. Both curves exhibit nearly identical sensitivities (slopes), indicating robustness to magnetic fields that are not aligned with the measurement direction. This can be explained by the increasing amplitude for one current direction and the decreasing amplitude for the other current direction in the measured anomalous Hall voltage, which almost perfectly cancels out the effect of external H_y bias fields. The offset changes from $o_x(\mu_0 H_y = 0\,\mathrm{mT}) = 50\,\mu\mathrm{T}$ to $o_x(\mu_0 H_y = 0.5\,\mathrm{mT}) = 76\,\mu\mathrm{T}$ in the presence of an external bias field in the y-direction. The sensitivity changes from $\xi_x(\mu_0 H_y = 0\,\mathrm{mT}) = 583\,\mathrm{V\,A^{-1}\,T^{-1}}$ to $\xi_x(\mu_0 H_y = 0.5\,\mathrm{mT}) = 557\,\mathrm{V\,A^{-1}\,T^{-1}}$.

For bias fields in the y- and z-directions, single-spin simulations were performed over various amplitudes up to $\pm 1\,\mathrm{mT}$ in each direction, as shown in Fig. 6. For every H_y and H_z bias field, a full H_x sweep was performed, as is visible in Fig. 5. This allowed the extraction of the sensitivity and offset data. The resulting sensitivities and offsets naturally depend on the strength of the SOT, determined by the SOT current and associated parameters, and in this case correspond to the experimental conditions shown in Fig. 2. In the case where both H_y and H_z bias fields were applied simultaneously, only simulations could be conducted, as the magnetic coils were limited to generating a 2D magnetic field. In Fig. 6(a) the sensitivity data ξ_x are visualized. The color code defines the amplitude of the data. On the x (y) axis the H_y-field (H_z-field) is varied. As can be seen, an H_y bias field does not change the slope a lot, which agrees with the measurement in Fig. 5(c). For higher H_y bias fields, the sensitivity decreases from $\xi_x = 577\,\mathrm{V\,A^{-1}\,T^{-1}}$ in the absence of a bias field to $\xi_x = 538\,\mathrm{V\,A^{-1}\,T^{-1}}$ at $\mu_0 H_y = 0.5\,\mathrm{mT}$. This reduction occurs because, as the external bias field increases, the SOT effect becomes less significant in comparison. As a result the magnetization of the FM layer will align with the external magnetic field and therefore decrease the SOT effect for both current directions. This will also lead to a decrease in the sensitivity, which can be observed in Fig. 6(a). This becomes noticeable above the linear range of the sensor, which is around

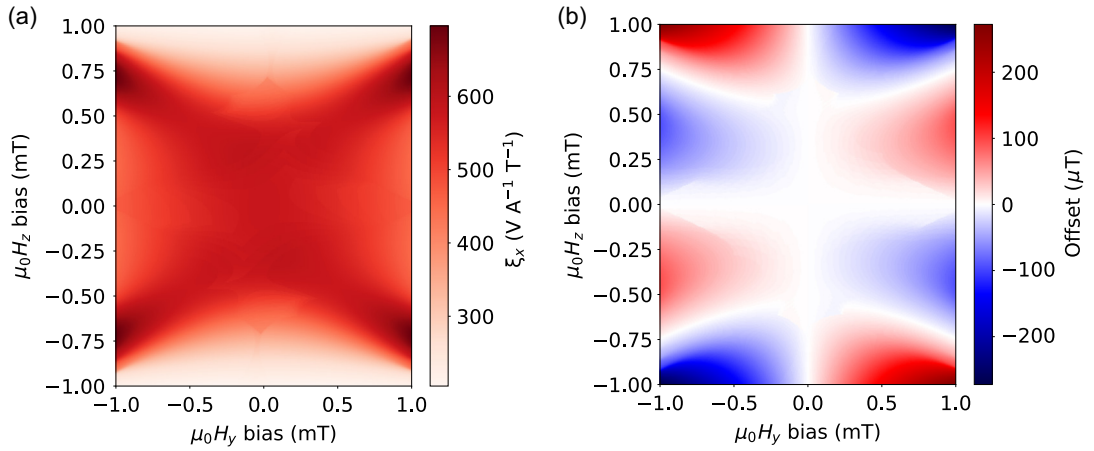

FIG. 6. (a) The simulated sensitivity (ξ_x) in units of V A^{-1} T^{-1} over external H_x-fields for different external bias fields in the y- and z-directions utilizing single-spin simulations. (b) The extracted offset values for different external bias fields in the y- and z-directions.

± 0.6 mT for IP fields. For the case of external $\mu_0 H_z$-fields the sensitivity drops significantly at bias fields just above 0.5 mT from $\xi_x = 577\,\mathrm{V\,A^{-1}\,T^{-1}}$ to $\xi_x = 301\,\mathrm{V\,A^{-1}\,T^{-1}}$ for $\mu_0 H_z = 0.8$ mT.

In Fig. 6(b) the simulated offset values for different bias fields can be seen. When the bias field is applied in only one direction (either the y- or z-direction), the offset remains zero. However, when the bias field has both y- and z-components, the offset becomes nonzero. For smaller external bias fields up to ± 0.6 mT (within the linear range), the offset remains relatively small (less than 50 μT). Beyond this range, the magnetization response to external fields is not linear anymore and therefore can not be utilized for detecting these fields. Despite this the simulation can still be performed successfully, and it appears that the offset begins to decrease again in the region from $\mu_0 H_y = 0.5$ mT to $\mu_0 H_z = 0.75$ mT, suggesting the onset of some compensation.

VII. DISCUSSION AND CONCLUSION

A 3D magnetic field sensor with offset compensation in all three dimensions has been shown. Utilizing a modulation principle of the magnetization via SOT, an offset performance of the order of tens of microteslas was achieved. For the measurement of the x-component of an external magnetic field with small (within the linear range of the sensor) H_y bias fields, no cross sensitivities were measured. An approach has been introduced to also measure the H_z-component without offset, employing a technique similar to the conventional spinning-current method in Hall effect sensors [15].

While the linear range of the present device is more limited compared to commercial sensors, strategies such as multilayer designs, alternative material stacks, or interface engineering could be employed to extend the linear regime. These approaches remain promising directions for future development, with the multilayer design already demonstrated in Ref. [27]. Such improvements are particularly relevant given the observed device instability and degradation over its operational lifetime.

The sensitive element is able to detect external magnetic fields in all three directions, without major cross sensitivities or changes in the offset, within a certain field range. If the amplitude of the bias field exceeds the linear range of the sensor (exceeding 0.6 mT for IP fields and 0.85 mT for OOP fields), then there is a noticeable change in the sensitivity and therefore in the signal.

The present study focused on the quasistatic behavior of the samples. While a full frequency-dependent characterization could provide additional insight, previous work on similar Ta/CoFeB/MgO/Ta devices [12] indicates that the noise is dominated by $1/f$ and Johnson contributions, suggesting that quasistatic measurement methods such as the spinning-current technique remain valid.

The magnetization state of the FM layer could not be fully determined experimentally. Attempts to capture magneto-optic Kerr effect images of the structure were not successful due to nontransparent layers on top of the sensitive structure. Consequently, the analytical extraction of the SOT parameters should be interpreted with caution, as it relies on the assumption of a single-spin system. Notably, the signs of the SOT parameters are the same, in contrast to the literature (see p. 31 in Ref. [16]), which reports opposite signs. Despite these limitations, the observed behavior was well reproduced by single-spin simulations. This method is expected to perform optimally for an IP FM layer consisting of a single domain and should inspire

researchers to extract the SOT parameters (η_{FL} and η_{DL}) from measurements, utilizing this approach.

VIII. METHODS

A. Sample fabrication

The samples examined in this work were produced on the same wafer with the same structure as those described in Ref. [10]. For the sake of completion, the production method is repeated here.

The SOT structure was produced on a 8-inch silicon wafer using a Singulus Rotaris system. Prior to depositing the three-layer film stack, an aluminum metallization layer was added to the wafer to establish electrical contact with the SOT structure from below. The aluminum layer was connected to the SOT structure through tungsten vias, separated by a SiO_2 insulating layer. A chemical mechanical polishing step was performed to smooth the surface before proceeding with the deposition of the SOT film stack. The stack consisted of Ta (6 nm)/$Co_{60}Fe_{20}B_{20}$ (1 nm)/MgO (1.5 nm)/Ta (5 nm) and was deposited using physical vapor deposition in a vacuum environment, with a base pressure of less than $5 \cdot 10^{-9}$ torr, ensuring no vacuum breaks between layers. Argon served as the sputtering gas for all the layers, with metal layers deposited in dc mode and the MgO layer in rf mode. After deposition, the wafers were annealed in a nitrogen atmosphere for 2 h at 280°C. The Hall bars used in this study were patterned from the films using conventional optical lithography and Ar ion etching. To protect the SOT structure from corrosion, a passivation layer was deposited. Further encapsulation, involving aluminum-filled vias around and metallization layers on top of the SOT structure, enhances heat dissipation. Finally, the pads were released by opening the passivation layer, and standard mechanical dicing techniques were used for separation.

B. Determination of R_s

To convert resistance values into the normalized magnetization in the z-direction (m_z), the anomalous Hall resistivity ρ_{xy} can be used [19]:

$$\rho_{xy} = R_0 H_z + R_s M_z. \tag{18}$$

$R_0 H_z$ represents the ordinary Hall resistivity, with R_0 denoting the ordinary Hall coefficient, while $R_s M_z$ represents the anomalous Hall resistivity, with R_s denoting the anomalous Hall coefficient. Because the ordinary Hall effect is almost always negligible compared to the AHE, the measured resistance R_{xy}, in the experiment, can be linearly correlated with the magnetization [28]:

$$R_{xy} \approx R_s m_z. \tag{19}$$

The AHE coefficient R_s was determined via the AHE resistance R_{xy} for a sample saturated in the z-direction.

For the calculation of the AHE coefficient the H_z measurement data were used, which can be seen in Fig. 2(f). The amplitude of S_z, in units of ohms, at highest applied external magnetic field was used ($S_z\,(\mu_0 H_z = \pm 40\,\mathrm{mT})$). This value was defined equivalent with $m_z = 1$ for a current density $j_e = 1.71 \cdot 10^{11}\,\mathrm{A\,m^{-2}}$ ($I_{xx} = 2.7\,\mathrm{mA}$), which leads to the AHE coefficient R_s:

$$\begin{aligned} R_s &= 0.5 \cdot [S_z\,(\mu_0 H_z = 40\,\mathrm{mT}) - S_z\,(\mu_0 H_z = -40\,\mathrm{mT})] \\ &= 0.687\,\Omega. \end{aligned} \tag{20}$$

This allows the conversion from resistance values in units of ohms to unit magnetization, which enables the direct comparison between experimental results and simulations, visible in Figs. 2(d)–2(f).

C. Measurement equipment

For the measurements the following equipment was used. To apply external magnetic fields, 2D coils from the company Brockhaus Messtechnik GmbH & Co. KG were used, powered by 2 Kepco power supply units. The power supply and measurement units for the test samples were provided by National Instruments. A PXIe-4139 SMU card was used as the power supply unit, while a PXIe-6366 card with a resolution of 2 MS/s served as the measurement unit. The entire experimental setup was connected to a computer, which controlled all operations. LABVIEW (National Instruments) was used to measure the samples and send commands to the power supply units. All measurements in this work were conducted using pulsed dc currents. For each value of the external magnetic field, both positive and negative SOT current pulses were applied. After sweeping through both current directions, the external field was incremented, starting and ending with a positive value. During each pulse, a dc current was applied to the test sample, and the measurement was performed. A short rest period followed each pulse. To minimize disturbances from time-varying magnetic fields, the external field was held constant throughout each pulse sequence.

D. Determination of current density in heavy metal

Since only the applied current in the Ta/CoFeB (HM/FM) bilayer is known, the current density within the HM layer, relevant for the SOT effect, must be calculated. As the individual layer resistivities were not measured, literature values are used for this purpose. For the Ta layer, which is in the β-phase, Ref. [29] reports a resistivity of approximately $\rho_{\mathrm{Ta}} = 200\,\mu\Omega \cdot \mathrm{cm}$ at a temperature of $T = 300\,\mathrm{K}$. Considering the sample heating due to high current densities, we assume a slightly reduced resistivity of $\rho_{\mathrm{Ta}} = 190\,\mu\Omega \cdot \mathrm{cm}$. For the CoFeB layer, Ref. [29] also provides a resistivity value of $\rho_{\mathrm{CoFeB}} = 100\,\mu\Omega \cdot \mathrm{cm}$. Using these two values and a two-resistors model, we get

the two resistances for the two individual layers with the equation

$$R = \frac{\rho \cdot L}{w \cdot t}. \tag{21}$$

Here ρ is the sheet resistivity, L the length of the Hall bar the current is traveling through, w the width of the Hall bar, and t the layer thickness. We have the following values: $L = 10\,\mu\text{m}$, $w = 2\,\mu\text{m}$, $t_{\text{Ta}} = 6\,\text{nm}$, and $t_{\text{CoFeB}} = 1\,\text{nm}$. The resistivities were already mentioned above. With Eq. (21) one obtains $R_{\text{Ta}} = 1583\,\Omega$ and $R_{\text{CoFeB}} = 5000\,\Omega$, which leads to a total resistance of $R_{\text{total}} = 1203\,\Omega$. This is close to the measured resistance of $R_{xx} = 1070\,\Omega$, visible in Fig. 3(a). Assuming ideal parallel conduction without interfacial resistance, the individual layer currents can be derived from the applied total current. In the measurements (see Fig. 2), a total current of $I_{xx} = 2.7\,\text{mA}$ was used. This leads to $I_{\text{Ta}} = 2.05\,\text{mA}$ and $I_{\text{CoFeB}} = 0.65\,\text{mA}$, with the current densities following from these values: $j_{\text{Ta}} = 1.71 \cdot 10^{11}\,\text{A}\,\text{m}^{-2}$ and $j_{\text{CoFeB}} = 3.25 \cdot 10^{11}\,\text{A}\,\text{m}^{-2}$. This means that for the case of an applied current of $I_{xx} = 2.7\,\text{mA}$ we have a current density of $j_{\text{Ta}} = 1.71 \cdot 10^{11}\,\text{A}\,\text{m}^{-2}$ flowing through the HM layer. Because the total resistance does not agree perfectly with the measured resistance the correct values could be a bit off and lead to slightly different SOT parameters [see η_{DL} and η_{FL} in Eq. (16)]. However, the exact value does not impact the validity of the results because the extracted SOT parameters, η_{DL} and η_{FL}, scale inversely with the applied current density [the p_f factor in Eqs. (A18) and (A19) in Appendix A]. Consequently, any variation in the simulated current density is exactly offset by a proportional adjustment in the extracted parameters. Put differently, doubling the current density would simply halve the SOT parameters, and vice versa. Therefore, the absolute value of the current density used in the simulation acts merely as a scaling factor and does not affect the fundamental physics or the interpretation of the extracted SOT parameters. It reflects the experimental situation of the data used for the extraction, which can be seen in Fig. 2.

ACKNOWLEDGMENTS

This research was funded in whole or in part by the Austrian Science Fund (FWF) [Grant No. 10.55776/I6267]. For open access purposes, the authors have applied a CC BY public copyright license to any author-accepted manuscript version arising from this submission. This project also received funding from Infineon Technologies Austria AG. In addition, F. Bruckner acknowledges funding from FWF under project no. 10.55776/PAT3864023. We gratefully acknowledge M. Kirsch and K. Prügl for their valuable assistance with sample fabrication.

Sebastian Zeilinger, F. Bruckner, S. Koraltan, J. M. Salazar-Mejía, and D. Suess developed and improved the single-spin and micromagnetic simulation codes. Sebastian Zeilinger and D. Suess derived the analytical solution. Sebastian Zeilinger, A. Satz, and J. Güttinger performed measurements at Infineon Technologies. Sebastian Zeilinger, B. Aichner, P. Heinrich, and Sophie Zeilinger carried out measurements at the University of Vienna. H. Brückl conducted measurements at the University for Continuing Education Krems. J. Güttinger, A. Satz, and D. Suess supervised the project.

Sebastian Zeilinger prepared the initial manuscript, and all authors contributed to the final version.

DATA AVAILABILITY

The data that support the findings of this article are not publicly available. The data are available from the authors upon reasonable request.

APPENDIX A: ANALYTICAL SOLUTION

The magnetization measured and simulated in this work can be described with an analytical equation which will be derived below. This approach assumes that the FM layer can be modeled as a single-spin system. If the spins are polarized in the y-direction, $\mathbf{p}$ can be represented as

$$\mathbf{p} = \begin{pmatrix} 0 \\ 1 \\ 0 \end{pmatrix}. \tag{A1}$$

The total effective field ($\mathbf{H}^{\text{eff,total}}$), including the DL and FL field, can be expressed as

$$\mathbf{H}^{\text{eff,total}} = \mathbf{H}^{\text{eff}} - H_{\text{FL}}\mathbf{p} - H_{\text{DL}}\mathbf{m} \times \mathbf{p}, \tag{A2}$$

with $\mathbf{H}^{\text{eff}}$ defined as

$$\mathbf{H}^{\text{eff}} = \mathbf{H} + \mathbf{H}_k, \tag{A3}$$

in which $\mathbf{H}$ denotes the contribution from external fields, and $\mathbf{H}_k$ is the effective anisotropy field, which in our case always points along the z-direction. The anisotropy field is defined as

$$\mathbf{H}_k = H_k\,(\mathbf{m} \cdot \mathbf{k})\,\mathbf{k}, \tag{A4}$$

with the anisotropy axis $\mathbf{k}$ pointing in our case in the z-direction [30], and the amplitude

$$H_k = \frac{2K_1}{\mu_0 M_s}. \tag{A5}$$

Here M_s is the saturation magnetization and K_1 the anisotropy constant. In equilibrium the total effective field

has to be parallel to the magnetization [see Eq. (5)]. In other words, $\mathbf{H}^{\text{eff,total}} = g \cdot \mathbf{m}$, which leads to

$$\begin{aligned} H_x + m_z \cdot H_{DL} &= g \cdot m_x, \\ H_y - H_{\text{FL}} &= g \cdot m_y, \\ H_z - m_x \cdot H_{\text{DL}} + m_z \cdot H_k &= g \cdot m_z. \end{aligned} \tag{A6}$$

Here m_i is the ith component of the magnetization unit vector and g a proportionality factor. Rearranging this equation yields

$$m_z = \frac{m_y H_z \left(H_y - H_{\text{FL}}\right) - m_y^2 H_x H_{\text{DL}}}{\left(H_y - H_{\text{FL}}\right)\left(H_y - H_{\text{FL}} - H_k m_y\right) + m_y^2 H_{\text{DL}}^2}. \tag{A7}$$

It is possible to replace H_{DL} and H_{FL}, utilizing Eq. (3):

$$m_z = \frac{m_y H_z \left(H_y - p_f\, \eta_{\text{FL}}\right) - m_y^2 H_x p_f\, \eta_{\text{DL}}}{\left(H_y - p_f\, \eta_{\text{FL}}\right)\left(H_y - p_f\, \eta_{\text{FL}} - H_k m_y\right) + m_y^2 {p_f}^2 \eta_{\text{DL}}^2} \tag{A8}$$

For small Gilbert damping and sufficiently strong positive current (I_{xx}^{+}), we assume values for η_{DL} and η_{FL} so that the magnetization almost points completely in the negative y-direction [31]:

$$\mathbf{m} = \begin{pmatrix} m_x \\ -1 \\ m_z \end{pmatrix}. \tag{A9}$$

A more detailed analysis of the equilibrium magnetization similar to Ref. [31] is given in Appendix B. This leaves us with the following expression for the z-magnetization for positive SOT current:

$$m_{z,I+} = \frac{-H_x \left|p_f\right| \eta_{\text{DL}} + H_z(\left|p_f\right| \eta_{\text{FL}} - H_y)}{\left(\left|p_f\right| \eta_{\text{DL}}\right)^2 + (\left|p_f\right| \eta_{\text{FL}} - H_y)(\left|p_f\right| \eta_{\text{FL}} - H_k - H_y)}. \tag{A10}$$

For negative current the magnetization will point in positive y-direction and also the signs of $\left|p_f\right| \eta_{DL/FL}$ change. This leaves us with

$$m_{z,I-} = \frac{H_x \left|p_f\right| \eta_{\text{DL}} + H_z(\left|p_f\right| \eta_{\text{FL}} + H_y)}{\left(\left|p_f\right| \eta_{\text{DL}}\right)^2 + (\left|p_f\right| \eta_{\text{FL}} + H_y)(\left|p_f\right| \eta_{\text{FL}} - H_k + H_y)}. \tag{A11}$$

Equations A10 and A11 can be combined into a single equation:

$$m_{z,I\pm} = \frac{\mp H_x \left|p_f\right| \eta_{\text{DL}} + H_z(\left|p_f\right| \eta_{\text{FL}} \mp H_y)}{\left(\left|p_f\right| \eta_{\text{DL}}\right)^2 + (\left|p_f\right| \eta_{\text{FL}} \mp H_y)(\left|p_f\right| \eta_{\text{FL}} - H_k \mp H_y)}. \tag{A12}$$

Now assuming vanishing H_y-fields, the equation becomes

$$m_{z,I\pm} = \frac{\mp H_x \left|p_f\right| \eta_{\text{DL}} + H_z(\left|p_f\right| \eta_{\text{FL}})}{\left(\left|p_f\right| \eta_{\text{DL}}\right)^2 + (\left|p_f\right| \eta_{\text{FL}})(\left|p_f\right| \eta_{\text{FL}} - H_k)}. \tag{A13}$$

By subtracting the solution for positive SOT current from that for negative SOT current, one can derive the analytical expression for the signal for external x-fields S_x:

$$\begin{aligned} S_x\,(H_x) &= \frac{R_s}{2} \cdot \left(m_{z,I+} - m_{z,I-}\right) \\ &= -R_s \frac{\eta_{\text{DL}} H_x}{-\eta_{\text{FL}} H_k + \left(\eta_{\text{DL}}^2 + \eta_{\text{FL}}^2\right)\left|p_f\right|}. \end{aligned} \tag{A14}$$

Similarly, by summing the two cases, the signal S_z for external z-fields can be obtained:

$$\begin{aligned} S_z\,(H_z) &= \frac{R_s}{2} \cdot \left(m_{z,I+} + m_{z,I-}\right) \\ &= R_s \frac{\eta_{\text{FL}} H_z}{-\eta_{\text{FL}} H_k + \left(\eta_{\text{DL}}^2 + \eta_{\text{FL}}^2\right)\left|p_f\right|}. \end{aligned} \tag{A15}$$

Utilizing the definition of the slopes [Eq. (12)], one obtains

$$\kappa_x = -\frac{\eta_{\text{DL}}}{-\eta_{\text{FL}} H_k + \left(\eta_{\text{DL}}^2 + \eta_{\text{FL}}^2\right)\left|p_f\right|}, \tag{A16}$$

$$\kappa_z = \frac{\eta_{\text{FL}}}{-\eta_{\text{FL}} H_k + \left(\eta_{\text{DL}}^2 + \eta_{\text{FL}}^2\right)\left|p_f\right|}. \tag{A17}$$

Rearranging these equations in terms of the SOT parameters η_{FL} and η_{DL}, one is left with the final equation utilized

for the extraction:

$$\eta_{\mathrm{FL}} = \frac{\kappa_z + H_k \kappa_z^2}{|p_f| \left(\kappa_x^2 + \kappa_z^2\right)}, \tag{A18}$$

$$\eta_{\mathrm{DL}} = \frac{-\kappa_x - H_k \kappa_x \kappa_z}{|p_f| \left(\kappa_x^2 + \kappa_z^2\right)}. \tag{A19}$$

APPENDIX B: EQUILIBRIUM MAGNETIZATION

Understanding the equilibrium magnetization under varying SOT strength is essential. To this end, we begin with the explicit Landau-Lifshitz-Gilbert-Slonczewski equation including SOT, as described in Ref. [17]:

$$\partial_t \mathbf{m} = -\frac{\gamma}{1+\alpha^2}\, \mathbf{m} \times \left[\mathbf{H}_k + (\alpha H_{\mathrm{DL}} - H_{\mathrm{FL}})\, \mathbf{p}\right] - \frac{\alpha\gamma}{1+\alpha^2}\, \mathbf{m} \times \left(\mathbf{m} \times \left[\mathbf{H}_k - \left(\frac{1}{\alpha} H_{\mathrm{DL}} + H_{\mathrm{FL}}\right) \mathbf{p}\right]\right), \tag{B1}$$

To obtain a representation independent of the magnitude of H_k, we introduce relative coordinates H_{DL}/H_k and H_{FL}/H_k, yielding

$$\partial_t \mathbf{m} = \left(\frac{\gamma H_k}{1+\alpha^2}\right) \left(-\mathbf{m} \times \left[\hat{\mathbf{e}}_z m_z + \left(\alpha \left(\frac{H_{\mathrm{DL}}}{H_k}\right) - \left(\frac{H_{\mathrm{FL}}}{H_k}\right)\right) \mathbf{p}\right] - \alpha \mathbf{m} \times \left(\mathbf{m} \times \left[\hat{\mathbf{e}}_z m_z - \left(\frac{1}{\alpha}\left(\frac{H_{\mathrm{DL}}}{H_k}\right) + \left(\frac{H_{\mathrm{FL}}}{H_k}\right)\right) \mathbf{p}\right]\right)\right). \tag{B2}$$

Here, $\hat{\mathbf{e}}_z = (0, 0, 1)$ denotes the unit vector in the z-direction. We now perform a rescaling of the time t to make both sides of the equation dimensionless. However, caution is required when H_k changes sign, as this would formally correspond to negative time evolution. To avoid this issue, we separate the sign and magnitude of H_k, treating $|H_k|$ in the prefactor and keeping the sign explicitly in the dynamics:

$$\begin{aligned} \partial_t \mathbf{m} = \left(\frac{\gamma\, |H_k|\, \mathrm{sgn}\,(H_k)}{1+\alpha^2}\right) \Bigg(&-\mathbf{m} \times \left[\hat{\mathbf{e}}_z m_z + \left(\alpha \left(\frac{H_{\mathrm{DL}}}{H_k}\right) - \left(\frac{H_{\mathrm{FL}}}{H_k}\right)\right) \mathbf{p}\right] \\ &-\alpha \mathbf{m} \times \left(\mathbf{m} \times \left[\hat{\mathbf{e}}_z m_z - \left(\frac{1}{\alpha}\left(\frac{H_{\mathrm{DL}}}{H_k}\right) + \left(\frac{H_{\mathrm{FL}}}{H_k}\right)\right) \mathbf{p}\right]\right)\Bigg). \end{aligned} \tag{B3}$$

We now define the rescaled time t' via

$$t' = t \cdot \left(\frac{\gamma\, |H_k|}{1+\alpha^2}\right). \tag{B4}$$

This rescaling allows for a unified treatment of cases where H_k is positive or negative, while always evolving the system forward in (rescaled) time. The resulting dimensionless equation is

$$\partial_{t'} \mathbf{m} = -\mathrm{sgn}\,(H_k) \cdot \left(\mathbf{m} \times \left[\hat{\mathbf{e}}_z m_z + \left(\alpha \left(\frac{H_{\mathrm{DL}}}{H_k}\right) - \left(\frac{H_{\mathrm{FL}}}{H_k}\right)\right) \mathbf{p}\right] + \alpha \mathbf{m} \times \left(\mathbf{m} \times \left[\hat{\mathbf{e}}_z m_z - \left(\frac{1}{\alpha}\left(\frac{H_{\mathrm{DL}}}{H_k}\right) + \left(\frac{H_{\mathrm{FL}}}{H_k}\right)\right) \mathbf{p}\right]\right)\right). \tag{B5}$$

Since we are only interested in the final equilibrium state and not the full time evolution, the specific value of t'_f merely determines when the system has relaxed. Equation (B5) is integrated using the `vode` solver from the SciPy library, configured with the backward differentiation formula method, across a range of values for H_{DL}/H_k and H_{FL}/H_k. The initial magnetization is set to $\mathbf{m}_{\mathrm{init}} = (1, 0, 0)$, which contrasts with Ref. [31], where the initial state pointed along the z axis. We use a rescaled time step of $\Delta t' = 0.1$, and integrate up to $t'_f = 100$. The damping parameter in our simulations is fixed at $\alpha = 0.05$, and a positive anisotropy field is assumed. References [20,21] report low damping around 0.01, varying with CoFeB thickness. The value $\alpha = 0.05$ is representative, and, as shown in Ref. [31], varying the damping parameter slightly does not significantly affect the simulation results. The remaining simulation parameters were kept unchanged and are listed at the end of Sec. III (Fig. 7).

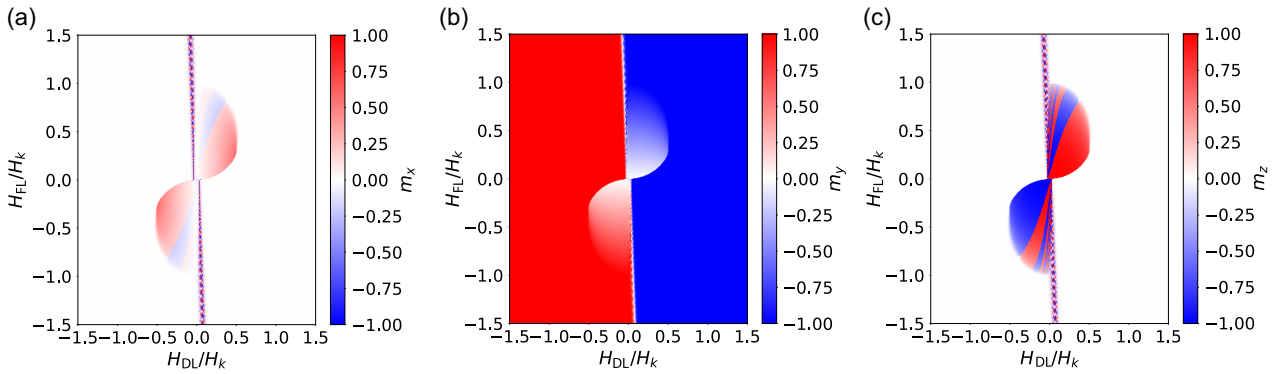

FIG. 7. Simulated equilibrium magnetization in the x- (a), y- (b), and z-direction (c) for different SOT strengths, normalized to the anisotropy field. Values range up to $\pm 1.5 \cdot H_{\mathrm{FL/DL}}/H_k$.

The results show that, for sufficiently strong SOT $\left(\left|H_{\mathrm{DL/FL}}/H_k\right| > 0.5\right)$, the magnetization predominantly relaxes into the y-direction. For positive values of the dampinglike torque the system relaxes mostly in the negative y-direction, agreeing with the assumption of the analytical solution (see Appendix A). The thin, nearly vertical features correspond to persistent magnetization oscillations, indicating nonconverging dynamics, consistent with the observations in Ref. [31].

APPENDIX C: ANISOTROPY FIELD EXTRACTION

To determine the optimal anisotropy field H_k, an iterative minimization scheme was employed based on minimizing the absolute error between measured and simulated signals under external fields H_x and H_z. Since the measured and simulated signals are subtracted from each other, a distinct nomenclature becomes necessary, even though they represent the same quantity.

1. Definitions

Let $S_x^{\mathrm{meas}}(H_{x,i})$ and $S_z^{\mathrm{meas}}(H_{z,i})$ be the measured signals, $S_x^{\mathrm{sim}}(H_{x,i}, H_k)$ and $S_z^{\mathrm{sim}}(H_{z,i}, H_k)$ be the simulated signals dependent on H_k, and $\mu_0 H_{x/z,i} \in [-10\,\mathrm{mT}, 10\,\mathrm{mT}]$ be a set of N_H equidistant external field points.

2. Error function

The total error for a given H_k is defined as the sum of absolute differences between simulated and measured signals:

$$\Delta(H_k) = \sum_{i=1}^{N_H} \left(S_x^{\mathrm{meas}}(H_{x,i}) - S_x^{\mathrm{sim}}(H_{x,i}, H_k)\right)^2 + \sum_{i=1}^{N_H} \left(S_z^{\mathrm{meas}}(H_{z,i}) - S_z^{\mathrm{sim}}(H_{z,i}, H_k)\right)^2. \quad \text{(C1)}$$

3. Optimization procedure

(1) Initialize a search interval for H_k: $[H_{k,\min}, H_{k,\max}]$.

(2) Choose the number of discrete evaluation points per iteration, N_k, and total number of refinement steps, n_{iter}.

(3) For each iteration $j = 1, \ldots, n_{\mathrm{iter}}$:

(a) Define N_k equidistant test points, $H_k^{(1)}, \ldots, H_k^{(N_k)}$, within the current interval.

(b) Evaluate $\Delta(H_k^{(i)})$ for all $i = 1, \ldots, N_k$.

(c) Identify the minimizing value:

$$H_k^* = \arg\min_{H_k^{(i)}} \Delta(H_k^{(i)}).$$

(d) Define a new narrower interval around H_k^*:

$$H_{k,\min}^{(j+1)} = H_k^* - \delta_j, \quad H_{k,\max}^{(j+1)} = H_k^* + \delta_j,$$

with $\delta_j = (H_{k,\max}^{(j)} - H_{k,\min}^{(j)})/N_k$.

(4) After the final iteration, the optimal anisotropy field is taken as:

$$H_k^{\mathrm{opt}} = H_k^*.$$

In this work we used $\mu_0 H_{k,\min} = 0\,\mathrm{mT}$, $\mu_0 H_{k,\max} = 100\,\mathrm{mT}$, $N_k = 20$, and $n_{\mathrm{iter}} = 5$.

APPENDIX D: TEMPERATURE INFLUENCE

Joule heating occurs due to the strong SOT currents and therefore requires careful investigation. To study this, R_{xy} was measured for one of the samples at different current strengths. The measurement employed pulsed dc currents with a pulse duration of $dt = 0.3$ s and a recording time of $t_r = 0.25$ s. The external magnetic field was swept between $\mu_0 H_{\mathrm{ext}} = \pm 40\,\mathrm{mT}$ in increments of 0.1 mT.

The data measured under OOP magnetic fields are shown in Fig. 8(a). The applied current amplitude was varied from $I_{xx} = 1.9\,\mathrm{mA}$ to $I_{xx} = 2.9\,\mathrm{mA}$, represented by a gradual change in color from dark purple (lowest current strength) to bright yellow (highest current strength). A

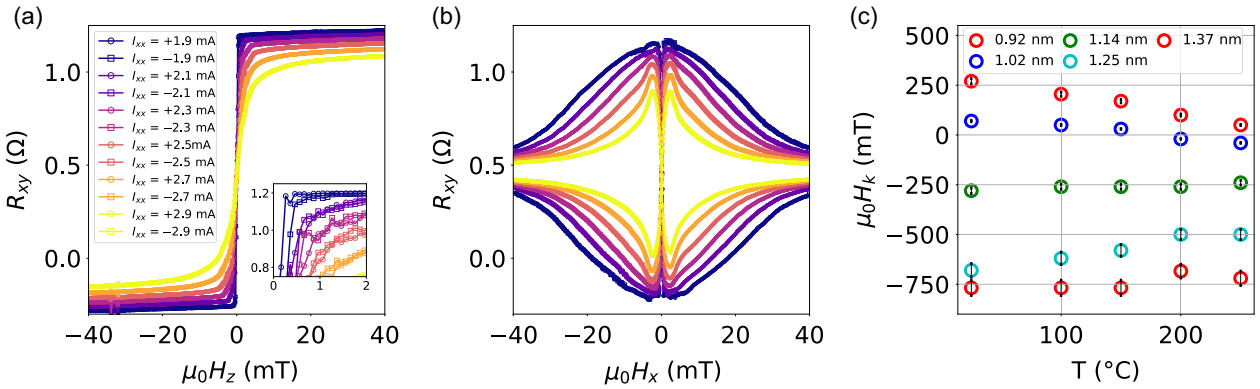

FIG. 8. (a) Measured R_{xy} values for different applied SOT currents along the x-direction (I_{xx}) under external OOP magnetic fields H_z. The region from $\mu_0 H_z = 0$ mT to $\mu_0 H_z = 2$ mT is shown enlarged at bottom right. (b) Measured R_{xy} values for the same SOT currents under external magnetic fields applied along the x-direction. (c) Measured effective anisotropy fields H_k as a function of temperature for different FM layer thicknesses in the stack Ta (6)/$Co_{60}Fe_{20}B_{20}$ (t_{FM})/MgO (1.5)/Ta (5).

decrease in the saturation magnetization due to Joule heating is observed. Both current directions were measured, with positive currents indicated by circles and negative currents by squares. This difference is more clearly visible in the enlarged plot from $\mu_0 H_z = 0$ mT to $\mu_0 H_z = 2$ mT, where a slight asymmetry between positive and negative current directions can be seen.

In Fig. 8(b), the measured R_{xy} data under an external magnetic field applied along the x-direction for the same SOT currents are shown. With increasing current, not only does the maximum amplitude decrease, but the shape of the curve also changes. This behavior can be explained by the decreasing magnetic anisotropy with rising temperature, with clear OOP characteristics gradually transitioning to a more IP magnetization. This observation is consistent with the experimentally measured anisotropy fields (H_k) shown in Fig. 8(c). The H_k values were measured as a function of temperature up to $T = 250°C$ for different FM layer thicknesses [Ta (6)/$Co_{60}Fe_{20}B_{20}$ (t_{FM})/MgO (1.5)/Ta (5)]. For these measurements, an external magnetic field was applied without SOT current, and the saturation point was taken as the anisotropy field. For $t_{FM} =$ 1.02 nm, the anisotropy field shows a transition from OOP to IP magnetization between $T = 150°C$ and $T = 200°C$, which corresponds approximately to the device temperature at the highest current. This also agrees with the extracted anisotropy for the sample analyzed in Sec. III. The change in anisotropy is further reflected in Fig. 8(a), where the measured data before saturation shift with increasing current. For higher current amplitudes, larger fields are required to reach complete saturation.

Applying the anisotropy field extraction algorithm to the data of the device shown in Figs. 8(a) and 8(b) for a SOT current amplitude of $I_{xx} = 2.7$ mA, with an external magnetic field swept between $\mu_0 H_{ext} = \pm 40$ mT, yields an anisotropy field of $\mu_0 H_k = 3.85$ mT, which is nearly identical to the value reported in Sec. IV. This shows low variation in device-to-device performance regarding the anisotropy field. For a higher SOT current ($I_{xx} = 2.9$ mA), the extracted anisotropy field decreases to $\mu_0 H_k = 2.50$ mT, demonstrating the reduction in anisotropy with increasing current strength.

[1] X. Chen, Y. Xu, X. Xie, Y. Guo, and Y. Huang, A novel Hall dynamic offset cancellation circuit based on four-phase spinning current technique, in *2015 China Semiconductor Technology International Conference*, Shanghai (IEEE, Piscataway, NJ, USA, 2015), pp. 1–3.

[2] M. Motz, U. Ausserlechner, M. Bresch, U. Fakesch, B. Schaffer, C. Reidl, W. Scherr, G. Pircher, M. Strasser, and V. Strutz, A miniature digital current sensor with differential Hall probes using enhanced chopping techniques and mechanical stress compensation, in *2012 IEEE SENSORS Conference*, Taipei, Taiwan (IEEE, Piscataway, NJ, USA, 2012), pp. 1–4.

[3] S. S. P. Parkin, C. Kaiser, A. Panchula, P. M. Rice, B. Hughes, M. Samant, and S.-H. Yang, Giant tunneling magnetoresistance at room temperature with MgO(100) tunnel barriers, Nat. Mater. **3**, 862 (2004).

[4] S. Yuasa, T. Nagahama, A. Fukushima, Y. Suzuki, and K. Ando, Giant room-temperature magnetoresistance in single-crystal Fe/MgO/Fe magnetic tunnel junctions, Nat. Mater. **3**, 868 (2004).

[5] J. Lenz and S. Edelstein, Magnetic sensors and their applications, IEEE Sens. J. **6**, 631 (2006).

[6] M. Vopalensky and A. Platil, Temperature drift of offset and sensitivity in full-bridge magnetoresistive sensors, IEEE Trans. Magn. **49**, 136 (2013).

[7] R. Mishra and H. Yang, Emerging spintronics phenomena and applications, IEEE Trans. Magn. **57**, 1 (2021).

[8] J. Ryu, S. Lee, K.-J. Lee, and B.-G. Park, Current-induced spin–orbit torques for spintronic applications, Adv. Mater. **32**, 1907148 (2020).

[9] Q. Shao, P. Li, L. Liu, H. Yang, S. Fukami, A. Razavi, H. Wu, K. Wang, F. Freimuth, Y. Mokrousov, M. D. Stiles, S.

Emori, A. Hoffmann, J. Åkerman, K. Roy, J.-P. Wang, S.-H. Yang, K. Garello, and W. Zhang, Roadmap of spin–orbit torques, IEEE Trans. Magn. **57**, 1 (2021).

[10] S. Koraltan, C. Schmitt, F. Bruckner, C. Abert, K. Prügl, M. Kirsch, R. Gupta, S. Zeilinger, J. M. Salazar-Mejía, M. Agrawal, J. Güttinger, A. Satz, G. Jakob, M. Kläui, and D. Suess, Single-device offset-free magnetic field sensing with tunable sensitivity and linear range based on spin-orbit torques, Phys. Rev. Appl. **20**, 044079 (2023).

[11] Z. Luo, Y. Xu, Y. Yang, and Y. Wu, Magnetic angular position sensor enabled by spin-orbit torque, Appl. Phys. Lett. **112**, 262405 (2018).

[12] R. Li, S. Zhang, S. Luo, Z. Guo, Y. Xu, M. Song, Q. Zou, L. Xi, X. Yang, J. Hong, and L. You, A spin–orbit torque device for sensing three-dimensional magnetic fields, Nat. Electron. **4**, 1 (2021).

[13] X. Chen, H. Xie, H. Shen, and Y. Wu, Vector magnetometer based on a single spin-orbit-torque anomalous-Hall device, Phys. Rev. Appl. **18**, 024010 (2022).

[14] D. Suess, J. Guettinger, A. Satz, and S. Zeilinger, Anomalous Hall sensor and anomalous Hall sensing method, U.S. Patent Application, Publication No. 20250044376 (2025).

[15] P. J. A. Munter, A low-offset spinning-current Hall plate, Sens. Actuators A: Phys. **22**, 743 (1990).

[16] A. Manchon, J. Železný, I. M. Miron, T. Jungwirth, J. Sinova, A. Thiaville, K. Garello, and P. Gambardella, Current-induced spin-orbit torques in ferromagnetic and antiferromagnetic systems, Rev. Mod. Phys. **91**, 035004 (2019).

[17] Claas Abert, Micromagnetics and spintronics: Models and numerical methods, Eur. Phys. J. B **92**, 120 (2019).

[18] Y. Hayashi, Y. Hibino, F. Matsukura, K. Miwa, S. Ono, T. Hirai, T. Koyama, H. Ohno, and D. Chiba, Electric-field effect on magnetic anisotropy in Pt/Co/Pd/MgO structures deposited on GaAs and Si substrates, Appl. Phys. Express **11**, 013003 (2017).

[19] N. Nagaosa, J. Sinova, S. Onoda, A. H. MacDonald, and N. P. Ong, Anomalous Hall effect, Rev. Mod. Phys. **82**, 1539 (2010).

[20] S. Iihama, S. Mizukami, H. Naganuma, M. Oogane, Y. Ando, and T. Miyazaki, Gilbert damping constants of Ta/CoFeB/MgO (Ta) thin films measured by optical detection of precessional magnetization dynamics, Phys. Rev. B **89**, 174416 (2014).

[21] B. Rana and Y. Otani, Anisotropy of magnetic damping in Ta/CoFeB/MgO heterostructures, Sci. Rep. **13**, 8532 (2023).

[22] S. Cho, S.-h. Baek, Y. Jo, and B.-G. Park, Large spin Hall magnetoresistance and its correlation to the spin-orbit torque in W/CoFeB/MgO structures, Sci. Rep. **5**, 14668 (2015).

[23] F. Bruckner, S. Koraltan, C. Abert, and D. Suess, magnum.np: A PyTorch based GPU enhanced finite difference micromagnetic simulation framework for high level development and inverse design, Sci. Rep. **13**, 12054 (2023).

[24] R. Lo Conte, E. Martinez, A. Hrabec, A. Lamperti, T. Schulz, L. Nasi, L. Lazzarini, R. Mantovan, F. Maccherozzi, S. S. Dhesi, B. Ocker, C. H. Marrows, T. A. Moore, and M. Kläui, Role of B diffusion in the interfacial Dzyaloshinskii-Moriya interaction in $Ta/Co_{20}Fe_{60}B_{20}/MgO$ nanowires, Phys. Rev. B **91**, 014433 (2015).

[25] A. Hubert and R. Schäfer, *Magnetic Domains: The Analysis of Magnetic Microstructures* (Springer, Berlin, 1998).

[26] A. V. Khvalkovskiy, V. Cros, D. Apalkov, V. Nikitin, M. Krounbi, K. A. Zvezdin, A. Anane, J. Grollier, and A. Fert, Matching domain-wall configuration and spin-orbit torques for efficient domain-wall motion, Phys. Rev. B **87**, 020402(R) (2013).

[27] S. Koraltan, R. Gupta, R. Peremadathil Pradeep, F. Kammerbauer, I. Kononenko, K. Prügl, M. Kirsch, B. Aichner, S. Helbig, F. Bruckner, C. Abert, A. O. Mandru, A. Satz, G. Jakob, H. J. Hug, M. Kläui, and D. Suess, Skyrmionic device for three dimensional magnetic field sensing enabled by spin-orbit torques, arXiv:2403.16725.

[28] S. B. Wu, T. Zhu, X. F. Yang, and S. Chen, The anomalous Hall effect in the perpendicular Ta/CoFeB/MgO thin films, J. Appl. Phys. **113**, 17C717 (2013).

[29] Q. Hao and G. Xiao, Giant spin Hall effect and magnetotransport in a Ta/CoFeB/MgO layered structure: A temperature dependence study, Phys. Rev. B **91**, 224413 (2015).

[30] D. Zhu and W. Zhao, Threshold current density for perpendicular magnetization switching through spin-orbit torque, Phys. Rev. Appl. **13**, 044078 (2020).

[31] D. Suess, C. Abert, S. Zeilinger, F. Bruckner, and S. Koraltan, Field-free switching of perpendicular magnetic elements by using two orthogonal sub-nanosecond spin–orbit torque pulses, Appl. Phys. Lett. **125**, 032401 (2024).